Synchrotron x-ray measurement and finite element analysis of residual strain in TIG welded aluminium alloy 2024

Preston, RV, Shercliff, HR, Withers, PJ, Hughes, DJ, Smith, SD and Webster, PJ

Synchrotron X-ray Measurement and Finite Element Analysis of Residual Strain in TIG Welded Aluminium Alloy 2024

R.V. Preston[1], H.R. Shercliff[1], P.J. Withers[2], D.J. Hughes[3], S.D. Smith[4], P.J. Webster[3]

[1] Department of Engineering, University of Cambridge, Trumpington St, Cambridge, CB2 1PZ, UK
[2] Manchester Materials Science Centre, University of Manchester, Grosvenor St, Manchester, M1 7HS, UK
[3] School of Computing, Science and Engineering, Salford University, Salford, M5 4WT, UK.

[4] TWI, Granta Park, Cambridge, CB1 6AL, UK

KEYWORDS

Synchrotron X-ray, finite element, aluminium alloys, aerospace, welding, residual stress & strain

ABSTRACT

Residual strains have been measured in a TIG butt-welded 2024 aluminium alloy plate using synchrotron X-ray diffraction. Novel 2-dimensional strain maps spanning the whole plate reveal steep gradients in residual stress, and provide detailed validation data for finite element analysis. Two variants of a finite element model have been used to predict the residual strain distributions, incorporating different levels of plate constraint. The model uses decoupled thermal and elastic-plastic mechanical analyses, and successfully predicts the longitudinal and transverse residual strain field over the entire weld. For butt weld geometries, the degree of transverse constraint is shown to be a significant boundary condition, compared to simpler bead-on-plate analyses. The importance of transverse residual strains for detailed model validation is highlighted, together with the need for care in selecting the location for line scans as a means for model validation. The residual stress is largest in the heat-affected zone, being equal to the local post-weld yield stress, though the strength increases subsequently by natural ageing. In addition, a halving of the diffraction line width has been observed local to the weld, and this correlates with the microstructural changes in the region.

1. INTRODUCTION

The development of welded structures in high strength aluminium alloys is of great importance in the aerospace sector, as an alternative to riveted structures. Tungsten inert gas (TIG) welding, laser welding and friction stir welding are all under consideration for 2000, 6000 and 7000 series aerospace alloys. These processes are also commercially important for aluminium alloys in the automotive and maritime sectors. Process modelling and detailed experimentation are both used to address the key issues in welding of aluminium alloys, including the retention of good post-weld microstructures and properties[1-6], and the control of residual stress and distortion[7-11]. For fusion techniques there is the added complication for high-strength alloys of hot cracking during welding[12-14].

Residual stress in welding is primarily caused by the transient thermal cycle in the vicinity of the weld[15]. Thermal expansion of material close to the intense heat source is constrained by the surrounding cooler material, and the metal yields easily due to its reduced strength. On cooling, the misfit in strain between the yielded and unyielded regions leads to residual tensile stress (predominantly parallel to the weld). Finite element methods are necessary to capture the coupling between the transient thermal history, the evolution in elastic-plastic properties at elevated temperature, and the consequent development of residual stress. Recent work has led to the development of such a model, for the prediction of residual stress in bead-on-plate welds in 2024 aerospace aluminium alloy[10,11]. In this paper, the model is adapted to the more practical situation of a butt weld, introducing complex issues of transient mechanical constraint. Detailed validation is an essential aspect of building any reliable process model. The paper also illustrates the technique of synchrotron X-ray strain mapping over an entire weld, which provides unparalleled detail for FE model validation.

2. MATERIAL AND PROCESSING

2.1 Material and Welding Procedure

The plate material used in this study was 3.2 mm thick 2024 aluminium alloy, conforming to aviation standards (nominal composition 4.35% Cu, 1.50% Mg, 0.60% Mn, 0.50% Fe, 0.50% Si, 0.25% Zn, 0.20% Zr 0.15% Ti and 0.10% Cr). This was supplied by ALCOA, in the T3 temper commonly used in aerospace (solution heat-treated, cold-worked and naturally aged). Butt welds

were produced between plates of length 160 mm and width 150 mm, with start and stop positions approximately 10 mm from the plate edges (Figure 1). To reduce the distortion during welding, copper bars of dimensions 450×65×5mm were clamped 10mm to either side of the joint line (shown in Figure 1, for the lower half only), with a large copper backing plate beneath the weld. This arrangement differed slightly from the clamping used for the bead-on-plate welds[10,11]. Welding was conducted using a constant current MIGATRONIC TIG Commander 400 AC/DC (Mark 3) power source. The welding torch was mounted on a Gullco KAT variable speed carriage, and the traverse speed was 2.5 mm/s. The electrode was ceriated tungsten 2.4 mm in diameter (conforming to AWS A5.12-92) with a 2.4 mm gap between the electrode and the work-piece, and with argon shielding gas and 2319 filler wire (Al-6.3% Cu). The welding current was 210A with a potential difference of 9.49V, as measured by an ARCWATCH monitoring system, giving a nominal power of 2000W. The welding frequency was set to 50 Hz with an AC balance of 85% electrode negative, 15% electrode positive. The weld width varied from 10mm at the start of welding to 11mm at the end.

2.2 X-ray synchrotron experiments

The use of diffraction to measure accurately changes in lattice spacing, and hence strain, is well established. The advantages of using synchrotron X-rays (or neutrons) over laboratory X-rays are increased intensity and higher energy, enabling penetration of large thicknesses and high spatial resolution. The advantages of synchrotron over neutron diffraction are: (i) smaller gauge volume, giving better spatial resolution, and (ii) faster measurements, enabling full strain mapping over the welded plate. Disadvantages include the lower diffraction angle with synchrotron X-rays, giving an elongated gauge volume, and a tendency to produce speckled diffraction patterns at small gauge volumes. The former limits the ability to resolve gradients in strains through the thickness of the plate using 1mm slits. The latter tends to prevent the use of much smaller slit sizes (e.g. 50μm) to reduce the gauge length along the beam because, unless the grain size is very small, insufficient grains diffract within the gauge volume to give a powder average. Duplicate neutron and synchrotron line scans on both bead-on-plate and butt welds in 2024-T3 have been shown to be in good agreement[9,16]. The much shorter sampling time opens up the possibility of collecting high spatial resolution area strain maps, favouring the use of synchrotron data for validation of the FE model. The experiments reported here were undertaken on line BM16 of the European Synchrotron Radiation

Facility (ESRF) in transmission geometry using a monochromated beam of wavelength 0.3098Å. For this wavelength the transmission through 3.2mm of aluminium is approximately 60% compared with less than 10^{-18} for Cu X-rays (1.54Å). The experimental arrangement is shown schematically in Figure 2, with the scattering axis horizontal. The beam defining slits were 1mm wide and 1mm high. The Bragg angle θ was approximately 7.3º so as to record the Al (311) diffraction peak. At this angle the diamond shaped nominal gauge was significantly longer than the thickness of the sample so that the complete thickness of the plate was sampled (the sampling gauge volume effectively being 1×1×3.2 mm). In such cases, where the nominal gauge volume is larger than the sampling gauge volume, artefacts can arise known as 'surface effects'. However the influence of these was minimised through the use of an analyser crystal[17]. The plate was oriented so as to align either the longitudinal or transverse directions of the plate along the strain measurement direction (parallel to the scattering vector **q**). In order to calculate strain from the measured lattice spacings it is necessary to know the stress free lattice spacing, d_0. Because of the local changes in microstructure brought about by the thermal history in the weld zone, it is not necessarily reasonable to assume a constant value of d_0 across the plate. As a consequence a thin 0.5 mm cross-sectional slice was electro-discharge machined from the mid-length of a plate welded under identical conditions. Measurements were taken at three different depths through-thickness (0.6, 1.6 and 2.6 mm). The values of d_0 measured at different lateral distances from the weld centre-line showed no significant variation ($<10^{-4}$). Consequently, measurements were made in an un-welded section of plate to determine reliable values of d_0 for the longitudinal and transverse strain directions. The errors in the lattice spacing values comprise random statistical peak fitting ($<10^{-4}$) errors, repeatable point to point grain sampling fluctuations ($\sim 1\text{-}2\times10^{-4}$) and systematic errors, which are estimated to be no more than 2×10^{-4}. Note that there may still be some uncertainty in d_0 for the weld metal, which has a different composition to the base metal, but contiguity in strain between the weld metal and the parent in both the longitudinal and transverse directions in Fig. 6 suggests the effect is small, since any error would affect both in the same sense.

Traditional residual strain measurements by diffraction focus primarily on the diffraction peak shifts which relate directly to the macro residual stresses. However the peak widths, quantified most simply in terms of the full width half maximum (FWHM), can also provide important insights. Line broadening can arise from many microstructural sources including mosaic size, intergranular strain

(type II) and microstrain (type III) arising from dislocations, precipitates and defects. The variation in FWHM was also therefore recorded, for the diffraction peaks used to record the longitudinal strain.

To complete a residual strain map, over 600 measurements of strain were recorded on one side of the weld centre-line in each measurement direction (longitudinal and transverse). Measurements were also taken as lateral line scans, with measurements at 1mm intervals near the weld and 4mm in the far field. Figure 1 shows the area of weld analysed, with the positions of the two line scans selected for detailed comparison with the FE predictions. Approximately 4 measurements were made per minute. The strains were converted to residual stresses in the plane of the plate using the multiaxial form of Hooke's Law:

$$\sigma_x = \frac{E}{(1+\nu)}\left[\varepsilon_x + \frac{\nu}{(1-2\nu)}(\varepsilon_x + \varepsilon_y + \varepsilon_z)\right], \quad \sigma_y = \frac{E}{(1+\nu)}\left[\varepsilon_y + \frac{\nu}{(1-2\nu)}(\varepsilon_x + \varepsilon_y + \varepsilon_z)\right]$$

According to Hooke's Law all three strains ε_x, ε_y and ε_z are required. However with such low diffracting angles ε_z is difficult to measure. Instead we have applied the plane stress assumption (i.e. taken σ_z to be effectively zero) as the plate thickness is only 3.2mm and the gauge samples the whole thickness. In this way ε_z can be inferred and σ_x and σ_y calculated from Hooke's Law.

Figure 3 shows a map of the measured residual stresses in the longitudinal direction, which have the greatest magnitude. In this and all subsequent maps of the weld, the upper half of the weld only is shown (due to symmetry), with the weld itself running from left to right along the bottom edge of the plot. The positions of the measurements are also indicated in Figure 3. The maximum residual stress is over 175 MPa, and lies at a distance 5-7mm from the weld centre-line. Microstructural changes are considered later, but this distance corresponds approximately to the region of the heat-affected zone near the fusion boundary in which maximum softening occurs during welding. While the initial yield stress of the material is 350 MPa, the minimum post-weld yield stress in the HAZ is half this value – that is, the maximum residual stress is roughly equal to the local as-welded yield stress.

3. FINITE ELEMENT MODELLING

3.1 Overview of thermal and mechanical models

The FE model consisted of sequential uncoupled thermal and mechanical analyses. The essential characteristics of the FE model are as follows – further details are reported in[10,16]. The finite element analyses were run using the ABAQUS commercial FE software. Shell elements were used, since the thickness was small compared to all other dimensions and the through-thickness normal stresses could be assumed negligible. The mesh contained approximately 2000 linear elements, of types DS4 (thermal analysis) and S4R (mechanical analysis). Symmetry meant that only half of the weld was modelled (Figure 1). A 3D model was used to capture the non-steady-state conditions along the weld length. The most significant thermal boundary condition was the thermal contact to the backing plate. The bead-on-plate model used a calibrated continuous rise in backing plate temperature. This was omitted for the butt welds, for which a constant sink temperature of 20^{o}C was used with a heat transfer coefficient of 1600 $Wm^{-2}K^{-1}$. The heat source radius was also increased to 4mm in the butt weld to reflect the greater width of the fusion zone in the butt weld (due to the addition of filler). Validation of the thermal model for bead-on-plate welds[10] was used to guide the choice of heat transfer conditions in the butt welds. Consistent thermal field validation, including the varying width of the fusion zone along the weld, was more difficult for the butt weld, mainly due to the complexity of adding filler material. Mechanical boundary conditions are discussed below.

Previous analyses with bead-on-plate welds have considered the effect of the temperature-dependent yield response on the predicted residual stress[10,11,16]. Heat-treatable aluminium alloys soften rapidly over the temperature range 200-400^{o}C, depending on the time-scale of the exposure to temperature. Data were obtained from two sources – the ASM handbook[18] (for a 10,000 hour hold), and data from ALCOA[19] for a wide range of hold times (extrapolated to a 10 second hold, representative of welding timescales). That the softening is not reversible (due to dissolution and coarsening of the hardening precipitates) is an important aspect, so a history-dependent yield response may be needed to provide an accurate physical description[11]. However, these analyses revealed that the dominant effect is the significant drop in yield stress between room temperature and 400^{o}C and above, while the choice of ASM versus ALCOA data, or inclusion of history-dependent yield behaviour, made only modest changes to the predicted residual strain or stress. This is because most of the plastic strain occurs at high temperature, where the different yield stress-temperature responses converge. This also allowed the use of a more computationally

efficient perfectly plastic yield response, since it was established that the low work hardening at temperature had little effect on the results.

In the current analyses, history-independent ASM data were used (being the most computationally efficient). ALCOA data (with or without history-dependence) would be more physically realistic, but have been shown to make only modest changes to the predictions in the bead-on-plate welds. The resolution of the experimental data and uncertainties in the model are therefore insufficient to discriminate between the different constitutive responses at this level of detail.

3.2 Adaptations to mechanical model for butt welding

The principal factor differentiating a bead-on-plate weld from a butt weld is the transverse constraint applied to the weld centre-line. For a bead-on-plate weld FE model the nodes on the weld centre-line are tied to the symmetry plane throughout the analysis (Figure 4a). For a butt weld configuration, the problem is more complex. Ahead of the arc, the plates are able to move apart laterally (depending on the degree of constraint imposed), while behind the newly formed weld the two plates are fixed together on the symmetry plane (Figure 4b). A number of different implementations of centre-line boundary conditions were tested numerically[16], first on bead-on-plate welds, and then with adaptations to treat butt welds.

For all welds, the first problem was to apply boundary conditions to represent the clamps. Three variants were explored: no restraint, fixed vertical (out-of-plane) restraint only, and vertical restraint by spring elements (with varying degrees of pressure and friction). These analyses indicated a very weak influence on the peak longitudinal residual stress, but a much stronger influence on the maximum out-of-plane distortion. Distortion is sensitive to many factors in welding, which is why residual stress (or strain) are more robust quantities for model validation purposes. Two variants were retained for the butt weld analyses:

Model A: fixed vertical with no transverse constraint;

Model B: stiff vertical springs with friction between clamp, plate and backing bar.

In both cases, the clamps were released after full cooling to simulate removal of the weld from the rig, and to allow unimpeded synchrotron measurement.

On the butt weld centre-line, a routine was then required for fixing nodes behind the melt pool to represent solidification. This was achieved by fixing nodes immediately behind the melt pool, at

equal time intervals after the initial 1 second dwell – the time steps corresponding to the traverse time of the arc over the length of one element. A second boundary condition was required for the butt weld centre-line due to the ability of the gap to open and close ahead of the weld, as is commonly observed for arc processes[20]. In-plane displacements on the weld centre-line were therefore allowed, but restricted to separation only. Nodes crossing the centre-line would otherwise lead to overlap, which is not physically possible (Figure 4b). Hence if contact was made, the transverse displacement was fixed to zero until either the contact force ceased to be compressive or the nodes were welded over.

The addition of filler material led to weld thickening of approximately 0.8mm. This was incorporated using an option to increase the thickness of prescribed shell elements. The first three elements from the centre-line had a thickness of 4.0mm, while the 4th ramped down from 4.0mm to the plate thickness of 3.2mm. The thickening was assumed to be symmetrical through-thickness, though in practice the V-shape of the melt pool and a shallow channel in the backing plate led to greater deposition on the top surface. Note that for computational simplicity the thicker material was imposed on the initial mesh, rather than modified progressively as welding proceeded.

Finally, it should also be noted that the edges of the welded plates were trimmed parallel to the weld (due to space restrictions in the diffraction hutch). After trimming, the plate had a width of 85mm on one side of the weld, and 100mm on the other. Since the residual stresses at these distances from the weld are low, any load redistribution on cutting is expected to be small so the asymmetry introduced by cutting would be negligible. However, to allow for any load redistribution, the FE model was also "cut" (i.e. nodes released after cooling) along the nearest element nodes, which were 83mm from the centre-line.

4. RESULTS AND DISCUSSION

4.1 Effect of centre-line constraint on predicted residual strain

A significant benefit of X-ray synchrotron diffraction is the rapid sampling time. This facilitated the mapping of residual strain over the entire welded plate area for the dimensions used in this work, providing a thorough validation of the FE models. Residual strain was chosen for model

validation, rather than stress, since strain was the quantity measured experimentally. Figures 5 and 6 show the longitudinal and transverse residual strains, respectively. In each case the predictions of models A and B are compared against the synchrotron data. The severity of the band of tensile longitudinal strain is greater using the stiff contact springs (Model B) preventing both out-of-plane and transverse movement, both in magnitude and width, but both models show broad agreement with the experimental data in Figure 5c. The differences in the models are much more marked in the transverse residual strains (Figures 6a,b). The model with transverse constraint (Model B) shows a lower level of compression 5-10mm from the centre-line, and a distinct region of transverse tension 20-30mm off the centre-line towards the centre of the weld. Comparison with the experimental map (Figure 6c) shows that this tensile region is observed in practice. Note that in both models the compressive and tensile transverse strains near the start and stop positions are well simulated.

Figures 5 and 6 illustrate that the degree of transverse constraint imposed has a significant influence on the predicted residual strains (and thus stresses). Model B which imposed stiff constraint both out-of-plane and in the transverse direction gives the best fit to the residual strain maps. The predictions for the constrained butt weld model are similar to our previous bead-on-plate model[16]. This is because well-clamped butt welds have little freedom of movement and thus behave in a similar manner to bead-on-plate welds, in which no displacement is possible normal to the joint-line. Numerically simpler bead-on-plate analyses may therefore be sufficient in some instances for a preliminary assessment of residual stress in butt welds.

The complete weld strain maps illustrate some important aspects of model validation. Firstly, there is no true steady-state region in the weld. For welds of this length the thermal field may be regarded as close to steady-state over a portion nearer to the start than the finish of the weld (between 40 and 80mm). Similarly, the consequent longitudinal strains show a long band of tension along the weld, which changes only slowly in width and magnitude. The transverse strains however vary continuously along the weld, with only a short region of perhaps 20-30mm where the strain field is essentially unchanging. An important consequence of this observation is the inherent uncertainty in model validation that relies solely on line scans. If the strains evolve with position along the weld, the conclusions drawn from a line scan can be sensitive to the exact position at which model and experiment are compared. Line scans are therefore best taken from

regions in which the strains are not changing rapidly, but this necessarily requires some prior knowledge of the overall stress field, or a complete 2D map.

Two sample line scans were extracted from both model and experiment, for positions 45 and 115mm along the welds, as illustrated in Figure 1. In these positions the strain fields are significantly different from one another, but there is little local change with respect to the welding direction. Figure 7 shows the comparison of the two models and the experiments, for both longitudinal and transverse residual strain. In each location, both models capture the overall shape of the longitudinal strain well. The more constrained model (B) over-predicts the peak tensile strain at x=45mm, but fits the compressive remote field more accurately. The more significant differences in the models are apparent in the transverse strains, where the more constrained model provides a much better fit. A compressive transverse strain at the weld centre-line is also apparent in the measurements in disagreement with the models. This feature may be an artifact of the experiments, caused by a failure to properly account for the variation in the strain-free lattice spacing in the filler metal, which has a different composition to the welded plate.

The lower magnitude transverse strains are less significant in terms of design against weld failure, but they provide a more sensitive test of model validity than the longitudinal strains. This further illustrates the benefits of using the detailed area synchrotron mapping technique, though with each map taking 2½ hours it does have an associated time/cost penalty.

4.2 Full width half maximum (FWHM) data

The diffraction peaks can be used to monitor the evolution of phases caused by welding either post-mortem, or in-situ[21]. More subtle effects are evidenced by the variation in FWHM over the whole area of measurement, as shown in Figure 8a. Firstly it should be noted that the peak widths are extremely narrow, especially in the weld region ($2\theta \approx 0.015^{o}$). Secondly the continuous decrease in FWHM from the edge of the HAZ to the fusion boundary suggests that significant microstructural changes are taking place.

Considering the above microstructural effects in turn, the grain size in the sample varies from as little as 20μm in the central equiaxed zone within the weld metal to as much as 100μm at the fusion boundary and in the as-received plate. It is not unusual to find finer grains in the equiaxed

central region of fusion zones in these alloys; indeed filler compositions have been developed to promote nucleation, resulting in fine-grained relatively untextured weld metal. It is therefore unlikely that grain size broadening is important as this is assumed to be negligible for grain sizes greater than 1μm[22]. Intergranular stresses are also probably insignificant in this problem – they will not arise either from elastic anisotropy between grains (as aluminium is nearly elastically isotropic) or from plastic anisotropy (as the plastic strains introduced into the as-received plate are relatively small). As a result it is likely that type III microstresses are the major cause of the observed line broadening[22]. With regard to these microstresses, dislocations and coherent precipitates introduce a localised straining of the lattice planes. In the HAZ, the initial hardening precipitates either coarsen or dissolve, with GP zones forming subsequently by natural ageing in regions where dissolution occurred. These changes will result in peak broadening as they cause a local distortion of the lattice. It is also well-documented that the broad peaks characteristic of a cold-worked material sharpen appreciably during recrystallisation[22]. Dislocations are introduced in alloy 2024-T3 by prior cold-work (used to accelerate ageing). The deformation is modest and is unlikely to trigger recrystallisation in the HAZ, but there may be some recovery during welding. The weld metal is of course undeformed.

Microstrain broadening is thus expected to depend either on dislocation recovery processes, or on the degree to which the lattice is distorted by precipitates. The FWHM may therefore be expected to correlate with the hardness or local yield stress after welding, which also depend on these factors (particularly precipitation state). The constitutive law developed to model the previous bead-on-plate welds[11] allowed for the history-dependence in the yield stress, due to dissolution and coarsening of hardening precipitates. This model infers the final room temperature yield stress, by using the peak temperature reached during the cycle to indicate the degree of permanent softening. Even though the history-dependent model was not used for the butt-weld analyses presented above, the peak temperature can still be used to infer the expected post-weld yield stress. Figure 8b shows the corresponding map of predicted post-weld yield stress. There is clearly a strong correlation with the FWHM data, suggesting that FWHM is effective in capturing the character of the microstructural changes induced by the elevated temperature excursion.

Figure 9a allows more quantitative analysis and shows a FWHM line scan at the position of one of the residual strain scans of Figure 7, together with the measured hardness (after post-weld natural

ageing). Figure 9b shows the corresponding predicted yield stress, immediately after welding, and the predicted peak temperature. The fusion boundary is clearly marked by the minimum in the FWHM. The FWHM variation is confined to the heat-affected zone, at the boundary of which it has attained the value representative of the parent plate. Comparison of the shape of the hardness profile (after natural ageing) with that of the post-weld yield stress profile indicates that significant strength recovery by natural ageing occurs in the HAZ, with a steep rise outside the fusion zone to a value close to that of the parent plate. This change does not appear to affect the FWHM (which was measured after natural ageing) as much as the changes during welding – the FWHM profile is close in shape to the yield stress immediately after welding. Further work is required looking at peak width changes during dissolution and ageing of the hardening precipitates to separate unambiguously the dislocation and precipitation effects.

5. CONCLUSIONS

Full-field synchrotron X-ray strain mapping has been undertaken of the longitudinal and transverse strains for a TIG butt weld joining two 2024-T3 aluminium alloy plates. The residual stresses were largest in the near-weld heat-affected zone. The maximum longitudinal residual stress is within the microstructurally affected zone (within 20mm of the weld centre-line) and is roughly equal in magnitude to the local yield stress. This stress is below the final minimum yield stress, due to subsequent natural ageing.

The strain maps confirm the importance of including appropriate levels of constraint in finite element models. In particular it is important to model the transverse constraints accurately; and in this respect the transverse strain map was useful in discriminating between models. A finite element model with strong constraint gave the best correlation with experimental strains. Indeed a previous bead-on-plate model captured most aspects of the weld stresses. Line scans are useful for quantitative comparisons between measurements and predictions, but when there is little or no steady-state region in a weld their location must be selected carefully, either on the basis of the finite element model or area strain maps.

The full width half maximum (FWHM) broadening of the diffraction peaks has been found to be sensitive to microstructural changes in the near weld zone, showing a high degree of correlation to the variation in both the measured hardness profile and a microstructural history-dependent FE model developed previously. The line width does not appear to change significantly upon

subsequent natural ageing, but decoupling the effects of dislocations and precipitation on FWHM requires further investigation.

ACKNOWLEDGMENTS

This project was funded by a DTI/EPSRC-funded post-graduate training partnership (PTP) between TWI and Cambridge University. Additional funding and provision of materials and welding facilities were provided by BAe Systems, Filton. The authors acknowledge the helpful discussions with Dr. Stewart Williams and Dr. Debbie Price of BAe Systems. Residual stress measurement was supported through an EPSRC/MOD joint grant and the experimental assistance of R.A. Owen is gratefully acknowledged.

REFERENCES

1. Grong Ø., *Metallurgical Modelling of Welding*, Institute of Materials, 1997, 2nd Edition.
2. Shercliff H.R. and Colegrove P.A., "Modelling of friction stir welding", in *Mathematical Modelling of Weld Phenomena 6*, (eds. H. Cerjak and H. Bhadeshia), Maney Publishing, Institute of Materials, UK, 2002, 927.
3. Grong Ø. and Shercliff H.R., "Microstructural Modelling in Metals Processing", *Prog. Mat. Sci.* 47, 2002, 163.
4. Myhr O.R., Grong Ø., Klokkehaug S., Fjær H.G. and Kluken A.O., "Process model for welding of Al-Mg-Si extrusions", *Sci. Tech. Weld. Join.* 2(6), 1997, 245.
5. Frigaard Ø., Grong Ø. and Midling O.T., "A Process Model for Friction Stir Welding of Age Hardening Aluminium Alloys", *Met. and Mater. Trans. A* 32A, May 2001, 1189.
6. Myhr O.R., Grong Ø., Klokkehaug S. and Fjær H.G., "Modelling of the microstructure and strength evolution during ageing and welding of Al-Mg-Si alloys", in *Mathematical Modelling of Weld Phenomena 6*, (eds. H. Cerjak and H. Bhadeshia), Maney Publishing, Institute of Materials, UK, 2002.
7. Myhr O.R., Klokkehaug S., Flaer H.G., Grong Ø. & Kluken A.O., "Modelling of Microstructure Evolution, Residual Stresses and Distortions in 6082-T6 Aluminium Weldments", *Welding Journal* 77, 1998, 286s.
8. Webster P.J., Djapic-Oosterkamp L., Browne P.A., Hughes D.J., Kang W.P., Withers P.J. and Vaughan G.B.M., "Synchrotron X-ray residual strain scanning of a friction stir weld", *J. Strain Analysis* 36(1), 2001, 61.
9. Owen R.A., Preston R.V., Withers P.J., Shercliff H.R. and Webster P.J., "Neutron and Synchrotron Measurements of Residual Strain in TIG Welded Aluminium Alloy 2024", *Mat. Sci. Eng. A*, 346(1-2), 2002, 159.

10. Preston R.V., Shercliff H.R., Withers P.J. and Smith S.D., "Finite Element Modelling of TIG Welding of Aluminium Alloy 2024", *Sci. Tech. Weld. Join*., 8(1), 2003, 10.

11. Preston R.V., Shercliff H.R, Withers P.J. and Smith S.D., "Physically-based Constitutive Modelling of Residual Stress Development in Welding of Aluminium Alloy 2024", *Acta Mater.* 52(17), 2004, 4973-4983.

12. Norman A.F., Drazhner V. and Prangnell P.B., "Effect of Welding Parameters on the Soldification Microstructure of Autogenous TIG Welds in an Al-Cu-Mg-Mn Alloy", *Mat. Sci. Eng*. A259, 2000, 53-64.

13. Norman A.F., Drazhner V., Woodward N. & Prangnell P.B., "Effect of Welding Parameters on the Microstructure of Al-Cu-Mg Autogenous TIG Welds", *Proc. 7th Int. Conf. on Joints in Aluminium (InAlCo99)*, Cambridge, UK, 1998, 29.

14. Prangnell P.B. & Norman A.F., "Grain Boundary Melting in Al-Cu-Mg Alloy Welds", *Proc. 6th Int. Conf. on Al Alloys (ICAA-6)*, Toyohashi, Japan, 1998, 1501.

15. Masubuchi K., "Residual Stresses and Distortion in Welds", *Encyclopedia of Materials: Science & Technology* (K.H.J. Buschow, R.W. Cahn, M.C. Flemings et al. Eds.), Elsevier, Oxford, UK, 2001.

16. Preston R.V., "Modelling of Residual Stresses in Welded Aerospace Alloys", PhD thesis, Cambridge University, UK, 2000.

17. Withers P.J., Preuss M., Webster P.J., Hughes D.J. and Korsunsky A.M., "Residual Strain Measurement by Synchrotron Diffraction", *Mat. Sci. Forum* 404-407, 2002, 1-12.

18. ASM, *American Society of Metals (ASM) Handbook*, *Aluminium and Aluminium Alloys* (ed. Davis J.R.), ASM International, Ohio, 1993 edition, 653-656.

19. ALCOA Research Laboratories, "Typical Mechanical Properties at Various Temperatures" ALCOA Internal Report, 1964-1970 (personal communication).

20. Masubuchi K, *Analysis of Welded Structures*, Pergamon Press, Oxford, 1980.

21. T. A. Palmer, J. W. Elmer, S. S. Babu, "Observations of Ferrite/Austenite Transformations in the Heat Affected Zone of 2205 Duplex Stainless Steel Spot Welds Using Time Resolved X-Ray Diffraction." *Mat. Sci. Eng.* A374, 2004, 307-321.

22. Cullity B D, *Elements of X-ray Diffraction*, Addison-Wesley, London, 1956.

Synchrotron X-ray Measurement and Finite Element Analysis of Residual Strain in TIG Welded Aluminium Alloy 2024

R.V. Preston[1], H.R. Shercliff[1], P.J. Withers[2], D.J. Hughes[3], S.D. Smith[4], P.J. Webster[3]

[1] Department of Engineering, University of Cambridge, Trumpington St, Cambridge, CB2 1PZ, UK

[2] Manchester Materials Science Centre, University of Manchester, Grosvenor St, Manchester, M1 7HS, UK

[3] School of Computing, Science and Engineering, Salford University, Salford, M5 4WT, UK.

[4] TWI, Granta Park, Cambridge, CB1 6AL, UK

FIGURE CAPTIONS

FIG. 1– Typical butt weld in 2024 aluminium alloy, showing FE mesh and location of copper clamps superimposed, and the location of line and area scans for synchrotron diffraction experiments. Welding direction from left to right. The inset figure shows the shape and size of the fusion zone cross-section halfway along the weld.

FIG. 2 – Side view of the experimental set-up for X-ray synchrotron diffraction experiments.

FIG. 3 – (x,y) map of the longitudinal residual stress, calculated from the measured residual strains.

FIG. 4 – Weld centre-line boundary conditions: (a) bead-on-plate; (b) butt weld.

FIG. 5 – Predicted and measured (x,y) maps of longitudinal residual strain for: (a) model A: low constraint butt weld model; (b) model B: strong constraint butt weld model; (c) synchrotron data.

FIG. 6 – Predicted and measured (x,y) maps of transverse residual strain for: (a) model A: low constraint butt weld model; (b) model B: strong constraint butt weld model; (c) synchrotron data.

FIG. 7 – A quantitative comparison between the predictions of the models and the measurements using line scans at positions along the welds of (a) x=45mm; (b) x=115mm.

FIG. 8 – (x,y) maps of (a) measured FWHM and (b) predicted post-weld yield stress.

FIG. 9 – Parallel line scan data for x=115mm: (a) measured FWHM and measured hardness after natural ageing; (b) predicted post-weld yield stress and peak temperature during welding.

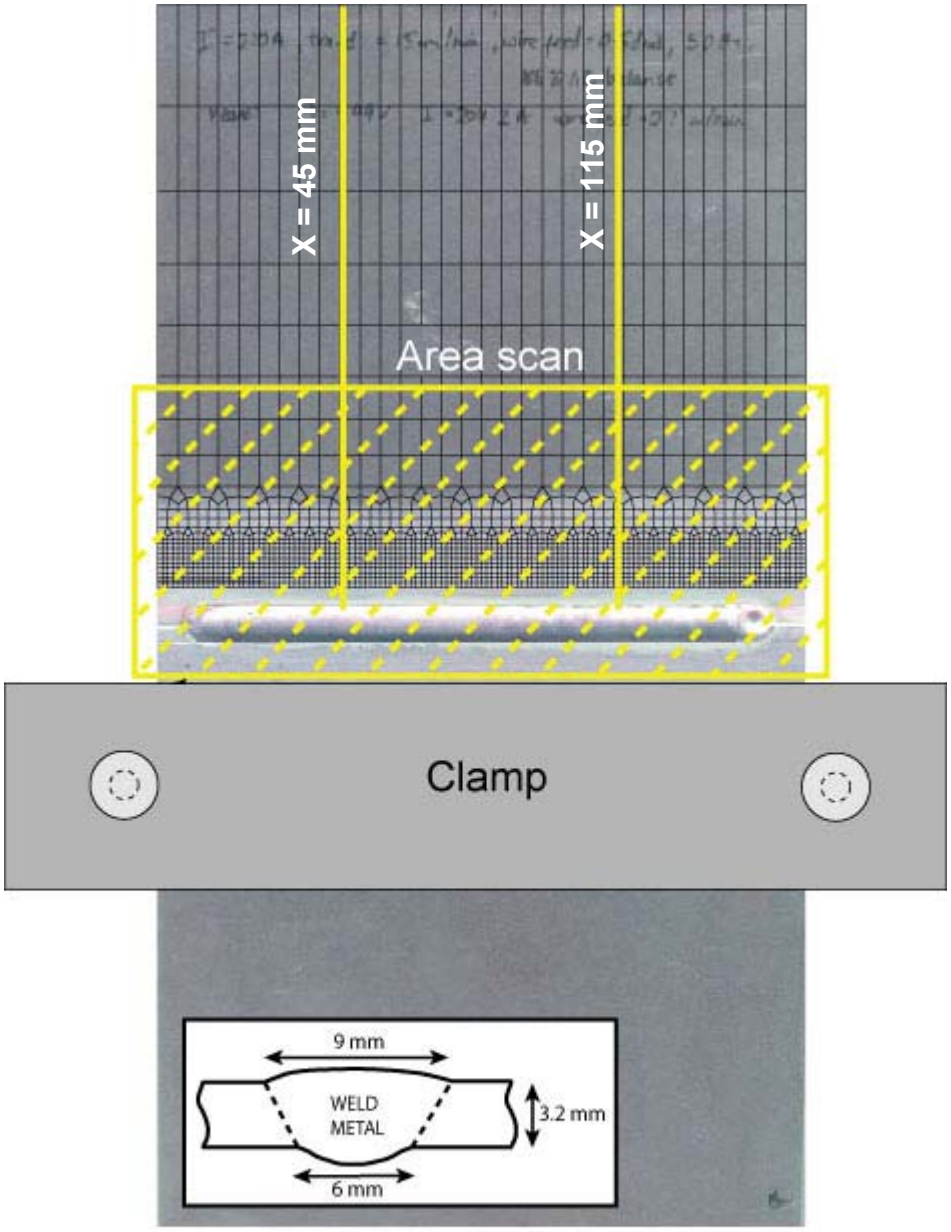

Figure 1

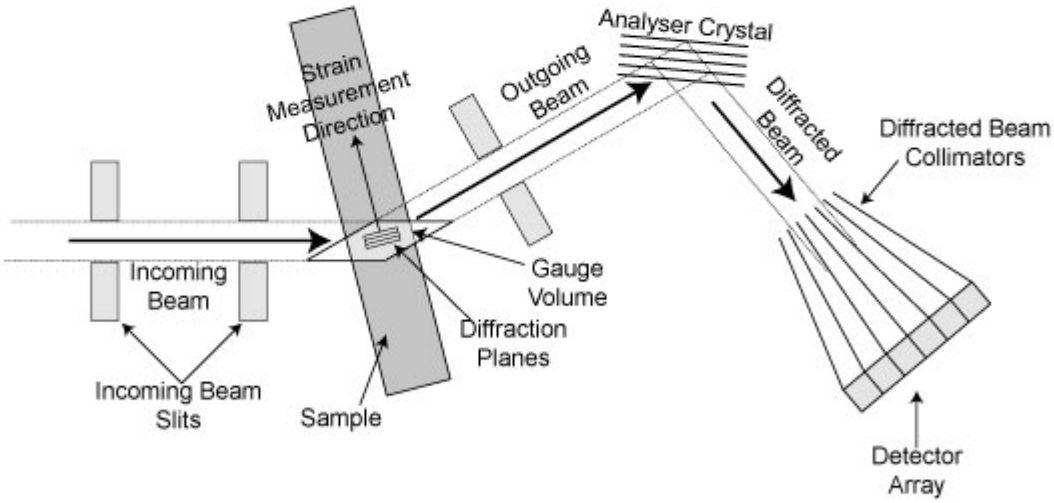
Analyser Crystal
Strain Measurement Direction
Outgoing Beam
Diffracted Beam
Diffracted Beam Collimators
Incoming Beam
Gauge Volume
Diffraction Planes
Incoming Beam Slits
Sample
Detector Array

Figure 2

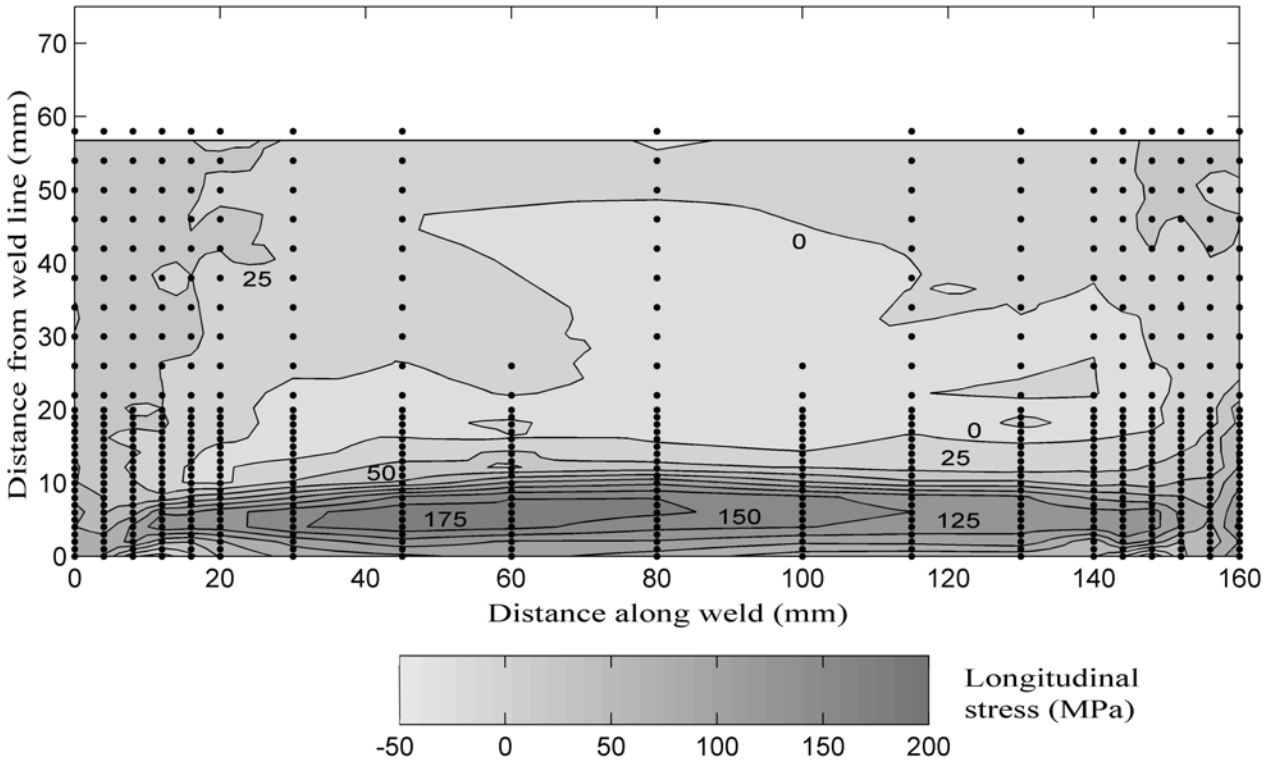
Distance from weld line (mm)
Distance along weld (mm)
0
25
50
175
150
125
0
25
0
20
40
60
80
100
120
140
160
0
10
20
30
40
50
60
70
-50
0
50
100
150
200
Longitudinal stress (MPa)

Figure 3

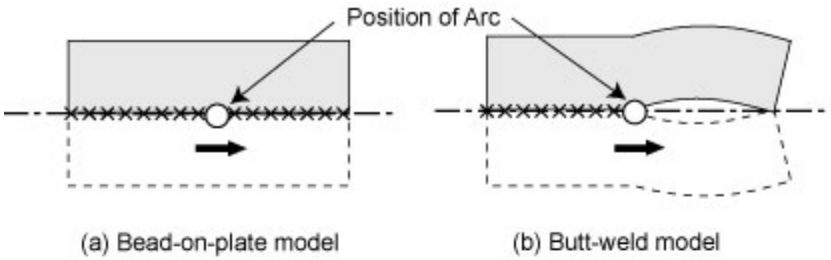

Figure 4

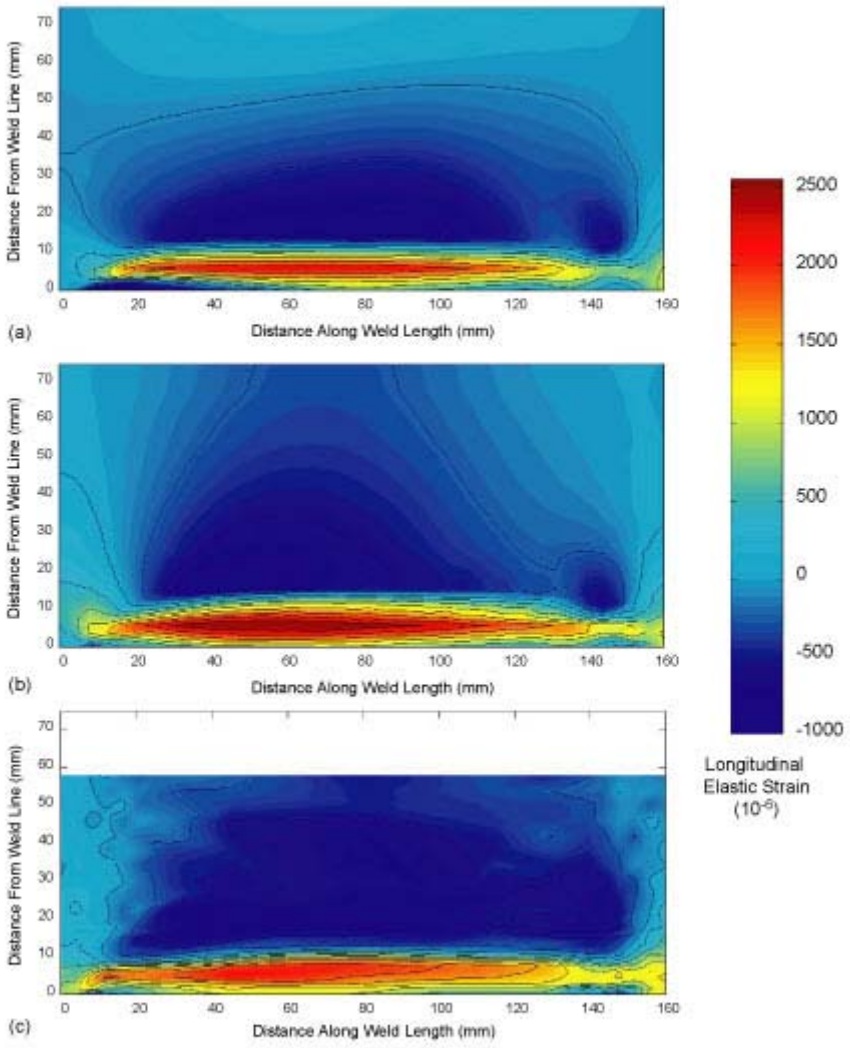
Distance From Weld Line (mm)
Distance Along Weld Length (mm)
(a)
(b)
(c)
2500
2000
1500
1000
500
0
-500
-1000
Longitudinal
Elastic Strain
(10^-6)

Figure 5

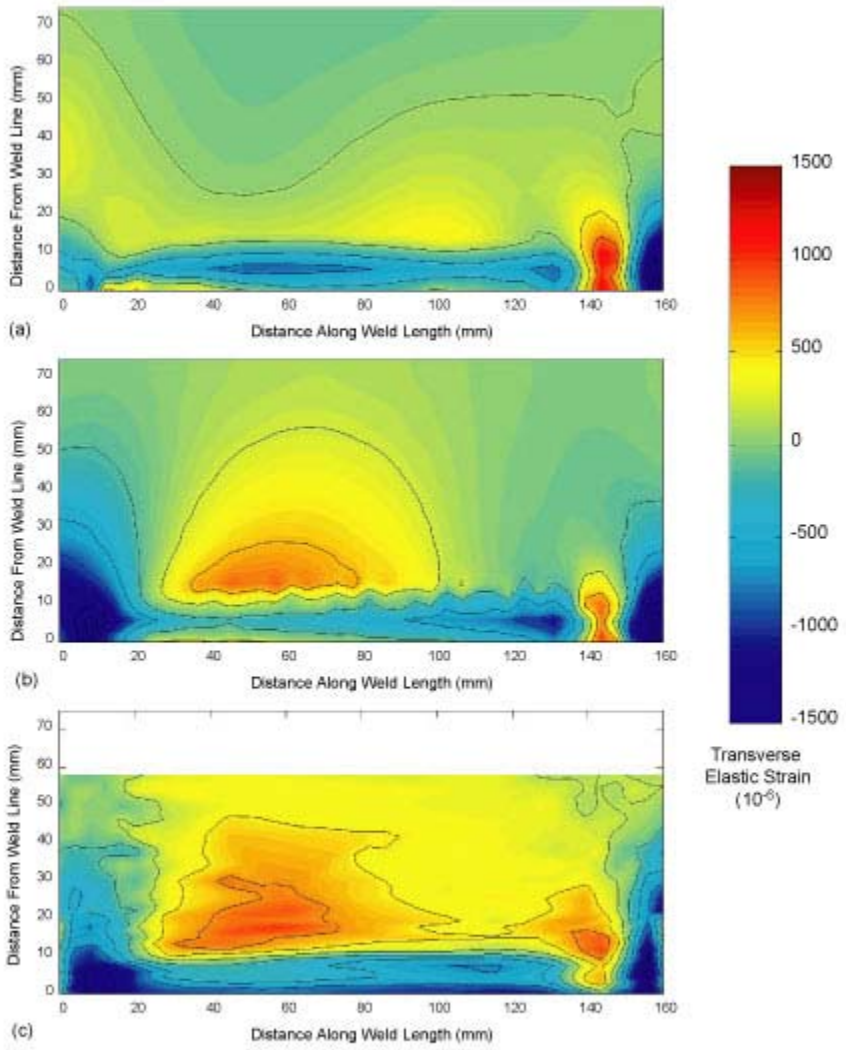
Distance From Weld Line (mm)
Distance Along Weld Length (mm)
(a)
(b)
(c)
1500
1000
500
0
-500
-1000
-1500
Transverse
Elastic Strain
(10^{-6})

Figure 6

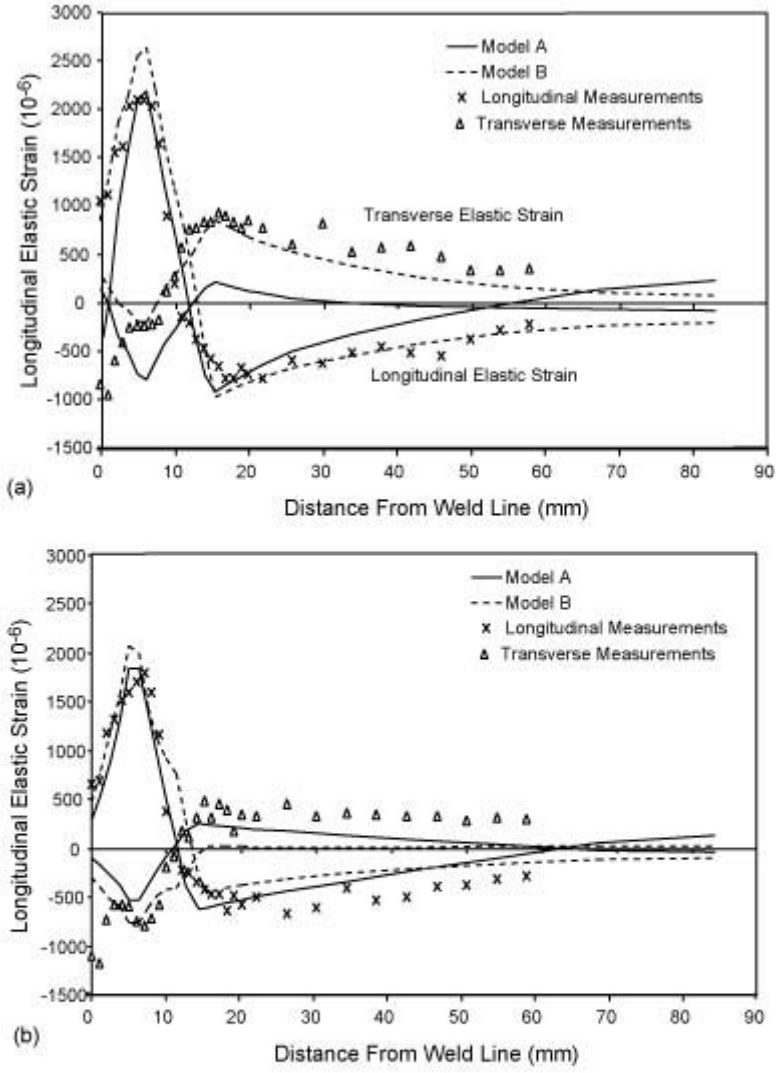
Model A
Model B
Longitudinal Measurements
Transverse Measurements
Transverse Elastic Strain
Longitudinal Elastic Strain
Longitudinal Elastic Strain (10⁻⁶)
Distance From Weld Line (mm)
(a)
(b)

Figure 7

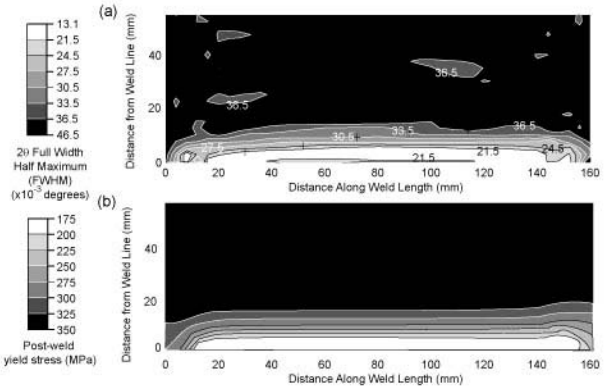
(a)
13.1
21.5
24.5
27.5
30.5
33.5
36.5
46.5
2θ Full Width Half Maximum (FWHM) (x10^-3 degrees)
Distance from Weld Line (mm)
Distance Along Weld Length (mm)
(b)
175
200
225
250
275
300
325
350
Post-weld yield stress (MPa)
Distance from Weld Line (mm)
Distance Along Weld Length (mm)

Figure 8

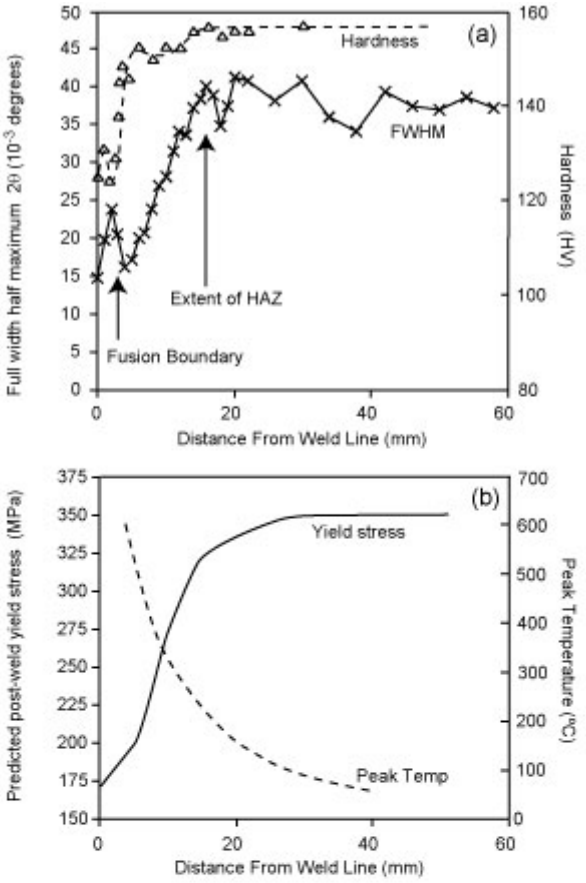
(a)
Hardness
FWHM
Extent of HAZ
Fusion Boundary
Full width half maximum 2θ (10^-3 degrees)
Hardness (HV)
Distance From Weld Line (mm)
(b)
Yield stress
Peak Temp
Predicted post-weld yield stress (MPa)
Peak Temperature (°C)
Distance From Weld Line (mm)

Figure 9